Precursor of transition to turbulence: Spatiotemporal wave front

S. Bhaumik* and T. K. Sengupta
Department of Aerospace Engineering, I.I.T. Kanpur 208 016, India†

(Received 4 August 2013; revised manuscript received 12 March 2014; published 28 April 2014)

To understand transition to turbulence via 3D disturbance growth, we report here results obtained from the solution of Navier-Stokes equation (NSE) to reproduce experimental results obtained by minimizing background disturbances and imposing deterministic excitation inside the shear layer. A similar approach was adopted in Sengupta and Bhaumik [Phys. Rev. Lett. **107**, 154501 (2011)], where a route of transition from receptivity to fully developed turbulent stage was explained for 2D flow in terms of the spatio-temporal wave-front (STWF). The STWF was identified as the unit process of 2D turbulence creation for low amplitude wall excitation. Theoretical prediction of STWF for boundary layer was established earlier in Sengupta, Rao, and Venkatasubbaiah [Phys. Rev. Lett. **96**, 224504 (2006)] from the Orr-Sommerfeld equation as due to spatiotemporal instability. Here, the same unit process of the STWF during transition is shown to be present for 3D disturbance field from the solution of governing NSE.

DOI: 10.1103/PhysRevE.89.043018 PACS number(s): 47.20.Ft, 47.27.Cn, 47.27.nb

I. INTRODUCTION

Transition to turbulence in fluid flow is still "the most important unsolved problem of classical physics" [1]. Whether turbulence is created deterministically or stochastically in fluid flow is still not decided categorically. But, in experiments turbulence is often created deterministically [2–5]. Wind tunnels are designed for transition research with very low background disturbances and an excitation source inside the boundary layer at a fixed frequency is often employed to cause transition. This aspect of causing transition of flows from laminar to turbulent state experimentally is related to receptivity of the former to certain classes of input disturbances. In Ref. [2], a vibrating ribbon placed perpendicular to the flow was excited monochromatically to create 2D disturbance wave-packet and the flow eventually became turbulent. Apart from validating the eigenvalues and egienfunctions of linear stability theories, such experiments also display features that cannot be explained by linear stability theories.

Tollmien and Schlichting predicted theoretically Tollmien-Schlichting (TS) waves, with parallel flow approximation of the linearized NSE [6] and the experiments in Ref. [2] was an attempt to validate this instability theory for the first time. When the similar experimental arrangement was simulated as an excitation problem, for space-time dependent disturbance field by Bromwich contour integral method [7], three elements of disturbance field are noted with the following structures: (i) a local solution followed by (ii) an asymptotic wave-packet and which is lead by (iii) the growing spatiotemporal wave front (STWF) [6]. The instability theory only predicts the asymptotic wave-packet in a qualitative manner. To replicate the experimental observations, one can follow the above linearized receptivity study [7] or solve the nonlinear NSE by direct numerical simulation (DNS) [6,8]. The results of a DNS is shown in Fig. 1, where a representative disturbance field obtained for a zero-pressure-gradient boundary layer perturbed by time-harmonic excitation is noted at a particular height. The growing STWF originating from the solution of OSE and by solving full 2D NSE is seen to be responsible for 2D transition [6,8]. In this respect, it is pertinent to distinguish the STWF from TS waves, the latter has been predominantly discussed in the literature. In Fig. 1, the time-accurate solution of NSE is displayed for the indicated physical parameters of excitation and nondimensional frequency $F = 2\pi\nu f/U_\infty^2 = 1.5 \times 10^{-4}$, for the physical frequency f in Hz and the indicated Reynolds number in the figure is defined by the local displacement thickness (δ^*) at the location of the exciter. In drawing this figure at a height of $y = 0.4747\delta^*$, computed NSE is for a Reynolds number, $\mathrm{Re}_L = 10^5$, based on an integral length scale (L) used for nondimensionalizing all lengths and U_∞ as the velocity scale. The result is shown for a time equal to $t = 18$.

It is to be noted that the STWF is not a mere transient, as it appears much later after the exciter is switched on and is related to spatiotemporal instability of the flow, dependent on the local shear layer property. Also, once the STWF is created inside a shear layer, it continues to grow, unlike other transient phenomena. The STWF was shown to originate theoretically from the solution of the receptivity problem given by the Orr-Sommerfeld equation, even when the boundary layer is excited at a location where the boundary layer is spatially stable [9], indicating its spatiotemporal growth has nothing to do with the traditional spatial instability analysis. STWF has never been reported by either temporal or spatial instability theories. Actual structure of the STWF was also shown to be similar by solving full 2D NSE [8], which helped track the nonlinear growth of the STWF to intermittent turbulent flow stage. However, to follow the nonlinear evolution of the STWF by NSE, the computational domain has to be long enough. For the presented results here, the domain length is five times more than that used in Ref. [10] to study 3D disturbance field. For the 2D turbulence simulation in Ref. [8], the computational domain is 12 times longer than that used in Ref. [10]. It is to be noted that in the context of spatiotemporal dynamics, 3D field is not a mere transformation of 2D results, as for spatiotemporal growth, one cannot use the Squire transformation linking two- and three-dimensional instabilities (useful for temporal instability only).

*swagata@iitk.ac.in
†http://spectral.iitk.ac.in

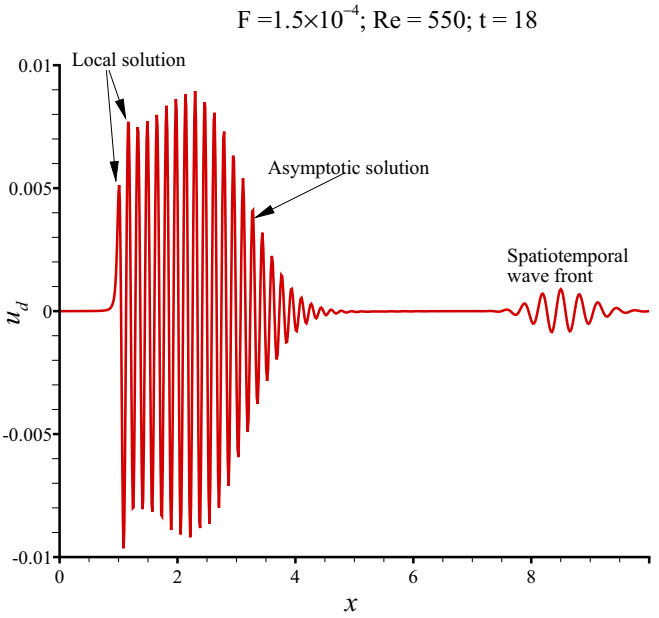

FIG. 1. (Color online) Streamwise disturbance velocity (u_d) plotted for a nondimensional frequency $F = 2\pi\nu f/U_\infty^2 = 1.5 \times 10^{-4}$, and a low amplitude of excitation ($\alpha_1 = 0.002$, i.e., a wall-normal maximum excitation velocity which is 0.2% of the free stream speed, U_∞). The result is shown at $t = 18$, for the exciter placed on the wall, where the Reynolds number based on local displacement thickness is Re = 550.

The STWF onset is by linear mechanism [9], which grows continually till the nonlinearity starts affecting the flow upstream to create adverse pressure gradient. Such adverse pressure gradient creates new STWFs in turn, all of which saturate nonlinearly. Self-regeneration is an essential property of the STWF, and this sequence of events continues once the STWF is created for an appropriate parameter combination. Two-dimensional transition in Refs. [8,11] is noted by tracking the STWF over a long computational domain. These references also clearly show that the TS wavepacket does not grow to create turbulence for moderate- to high-frequency excitations. Instead, the STWF is the main precursor for transition to 2D turbulence, with detailed processes dependent on frequency and amplitude of excitation. It is necessary to investigate whether 3D disturbance field also evolves into turbulence following the same unit process of the STWF. This is performed here by accurate simulations, minimizing all possible error sources. We review the various formulations of the Navier-Stokes equation in Appendix A and the numerical methods used by previous authors and methods, which are used here and explained in Appendix B.

The present paper is formatted in the following manner. In Sec. II, we explain how spatiotemporal structures are created inside boundary layer with respect to 2D boundary layer and a 1D model equation. Different routes of transition, explored via 3D simulations are described in Sec. III. Section IV focuses upon the receptivity of the zero-pressure-gradient boundary layer with respect to an excitation field created by a Gaussian circular patch on the surface of the plate in creating various vortical structures and turbulent spot formation during the transition process. In the last subsection, the energy spectrum of the inhomogeneous turbulent flow created by the wall excitation is shown and compared with relevant experimental results. The paper closes with concluding remarks in Sec. V.

II. SPATIOTEMPORAL STRUCTURE OF DISTURBANCE FIELD

To understand the structure of the STWF, consider the 1D convection diffusion equation,

$$\frac{\partial u}{\partial t} + c\frac{\partial u}{\partial x} = \nu\frac{\partial^2 u}{\partial x^2},$$

in an unbounded domain with the initial condition prescribed as $u(x,0) = f(x)$. Using bilateral Laplace transform [7], the spectrum of the initial condition is given as

$$\phi(\alpha) = \int f(\xi)e^{-i\alpha\xi}\, d\xi.$$

One gets the solution with $\alpha = \alpha_r + i\alpha_i$ as

$$u(x,t) = \frac{1}{2\pi}\int_{Br_\alpha}\int_{-\infty}^{+\infty} f(\xi)\, e^{i\alpha(x-\xi-ct)}\, e^{-\nu\alpha^2 t} d\alpha\, d\xi,$$

where Br_α is the Bromwich contour in the complex α plane [6]. The wavepacket nature is due to $e^{-\nu(\alpha_r^2-\alpha_i^2)t}$, and the phase of the packet changes according to $\alpha_r(x - ct - 2\nu\alpha_i t)$. This helps in explaining the role of diffusion in creating a wavepacket and not waves. Similarly, the amplitude of the STWF decreases and its width increases due to diffusion. The dynamics of the convected STWF is determined by the competition between diffusion and growth determined by the dispersion relation, $\omega = \alpha c - i\nu\alpha^2$.

In Ref. [6] it has been shown in the linearized parallel receptivity framework, that the disturbance field corresponds to the imposed wall excitation $v_d(x,0,t) = \delta(x)\, e^{i\omega_0 t} H(t)$, given by

$$v_d(x,y,t) = \left(\frac{1}{2\pi}\right)^2 \int_{\alpha,Br}\int_{\omega,Br}\left[\frac{i}{(\omega-\omega_0)}\right]$$

$$\left[\frac{\phi_3(0)\phi_1(y) - \phi_1(0)\phi_3(y)}{\phi_1(0)\phi_3'(0) - \phi_3(0)\phi_1'(0)}\right] \exp\left[i(\alpha x - \omega t)\right] d\alpha\, d\omega, \quad (1)$$

where $H(t)$ represents the Heaviside function due to finite start-up of the excitation, $v_d(x,y,t)$ represents the disturbance wall-normal velocity component, ω_0 is the excitation frequency, and α and ω are complex wavenumber and circular frequency, respectively. Here, $\phi_1(y)$ and $\phi_3(y)$ are the two fundamental solutions of OSE, which decay in the free stream ($y \to \infty$). The integrations in Eq. (1) are carried out along appropriately chosen Bromwich contours in α and ω planes as described in Ref. [9]. One notes from Eq. (1) that all complex frequencies centered around ω_0 are excited. The STWF created due to this time-harmonic excitation is therefore a linear combination of spatiotemporal eigenmodes of OSE with a weight proportional to $1/(\omega - \omega_0)$. The constituent eigenmodes of the STWF are spatiotemporal in nature, with both α and ω being complex.

III. DIFFERENT ROUTES OF 3D TRANSITION

Despite an early failed attempt [12] to create flow transition by 3D wall excitation, subsequent experiments on 3D

transition showed different vortical structures in the late stages of transition [3,4,13]. In these experiments, a rectangular ribbon with spanwise spacers is vibrated monochromatically near a flat plate, with resulting disturbance evolving into vortices with an appearance resembling the letter Λ, which are aligned and attributed to K-type transition in honor of Klebanoff [3], where the frequency of excitation in the experiments was 1489 Hz and above. In later experiments in the USSR, it was noted that the vortices in the nonlinear stage of evolution are staggered for lower frequencies, and the frequency of excitation was 120 Hz in Ref. [4]. Such a route of transition is associated to H-type transition, named after the proponent of another theoretical model. However, the main difference between the experiments in Refs. [3] and [4] is the excitation frequency. Corresponding computational and theoretical approaches did not use this observation on difference of frequency of excitation and instead H-type breakdown is attributed to a resonant mechanism, where a 2D disturbance wave interacts with two oblique waves having half the frequency of the 2D wave [14]. Here we note that this distinction between K- and H-type transition is not very relevant, as a growing boundary layer supports wavepackets and not waves. Despite this, in some computational efforts [10,15,16], authors have tried to detect H-type breakdown by an exciter vibrated at a fundamental and its subharmonic frequencies, simultaneously by wall-normal perturbation. In Ref. [10], additional nonphysical random white noise is added with the wall-excitation, purportedly to "encourage flow randomization and asymmetry in post-transitional turbulent region." In the present work, results from DNS show that different arrangements of vortices are due to frequency of excitation, following similar deterministic excitation strategy used in Ref. [2].

In computational efforts, the role played by the TS wavepacket is always highlighted [10,15–17]. Here, we show that the STWF is created by a 3D wall excitation, and apart from being the main precursor of transition, it follows different routes of transition depending upon amplitude and frequency of excitation. Present computations performed over a streamwise extent, which is five times longer than that in Ref. [10], display different dynamics for different routes of transition, all featuring the STWF. This implies that the STWF is relevant in the disturbance field for both 2D and 3D transition to take the flow from the excitation to the final turbulent stage.

Other complimentary views on *nonmodal transient growth* of *optimal* initial perturbations [18] may not be important, as the mechanisms are not generic to explain 2D and 3D routes of transition [19,20]. Also, the results do not support experimental observations on flow transition [2–4,13]. The growth associated with the STWF obtained from the solution of full NSE, as a response to harmonic wall excitation, helps in explaining 2D transition [8,11] and the present effort shows the same for 3D transition.

IV. 3D RECEPTIVITY OF BOUNDARY LAYER TO WALL EXCITATION

To explore the role played by the STWF for a 3D disturbance field, NSE is solved using DRP methods reported in Ref. [21]. Schematic of the computational domain used here is shown in Fig. 2(a), with the shear layer excited by a Gaussian circular patch (GCP) vibrated time-harmonically with the exciter periodic in the spanwise direction, with a period of $z_{\max}$. This excitation creates planar and oblique 3D TS wavepackets. Most 3D experiments are for time-harmonic spanwise modulated (SM) exciter, which is also computed, but not presented here, as the unit process appears to be the same. Imposed wall-normal velocity by the exciter is given by, $v_{\text{wall}}(x,z) = \alpha_1 A_m(x,z) H(t) e^{i\omega_0 t}$, where α_1 and ω_0 denote the amplitude and the frequency of excitation. Here, $H(t)$ is the Heaviside function needed for the impulsive start of excitation and $Maximum(|A_m(x,z)|) = 1$. The amplitude of the GCP exciter varies as $A_m = [1 + \cos(\pi r/r_{\max})]/2$, where $r_{\max}$ is the radius of the circular patch. Spanwise periodic conditions imply existence of exciters at a periodic interval of $z_{\max}$. The computational domain taken here is similar to Refs. [10,15,17], but significantly longer to allow full nonlinear evolution of the STWF in the computational domain. Also, the present computations do not use any random wide-band excitation and use strictly two-level time integration method, which does not have spurious numerical mode(s) [21].

The perspective view of the streamwise disturbance velocity (u_d) is shown in the (x,z) plane, in Fig. 2(b) at $t = 15$ for GCP exciter, with $\alpha_1 = 0.01$ and $z_{\max} = 1$. The nondimensional frequency is $F = 0.5 \times 10^{-4}$, where $F = 2\pi\nu f/U_\infty^2$; ν is the kinematic viscosity and f is the frequency of excitation in Hertz. Figure 2(b) identifies the three elements of response, as was shown in Refs. [8,9,11] for the creation of 2D turbulence. Following the local solution, planar and a pair of oblique TS wavepackets are seen in Fig. 2(b). For this case, leading the disturbance structure is the STWF, which grows rapidly, as was noted in 2D disturbance field [8,11]. Spatiotemporal growth of the disturbance field is shown in a plan view in Figs. 2(c)– 2(f), for the streamwise disturbance velocity, u_d, in a plane located at a nondimensional height of $y = 0.00215$. One notes higher wavenumber fluctuations (turbulent spots) at selected locations near the spanwise boundaries, due to interactions between neighboring STWFs, with disturbance levels of the order of U_∞. Two such zones (S_1 and S_2) identifying turbulent spots [Figs. 2(d) and 2(e)] are shown at $t = 26$ and 29. Here, these spots spread in both the streamwise and spanwise directions, while spawning newer spots upstream (S_3 and S_4), as shown in Fig. 2(e). This regeneration and self-induction mechanism establishes a fully turbulent zone extending from $x \simeq 13$ to 25 at $t = 36$ in Fig. 2(f).

A. Vortical structure formation during transition

During the secondary and tertiary stages of transition, various arrangements of vortical structures are noted and based on which transition processes are classified as belonging to K- and H-type transition routes. As mentioned earlier, with accurate computations all these arrangements are noted to depend upon the frequency of excitation alone, with the K-type breakdown noted for higher-frequency excitation. In Fig. 3, we have plotted the plan view of $\lambda_2 = -0.005$ isosurface (colored by streamwise velocity) for the GCP exciter case of Fig. 2(b). Here λ_2 is the second eigenvalue of the symmetric matrix formed by the symmetric and the antisymmetric part of the rate of strain or velocity gradient tensor [22]. Negative values of λ_2

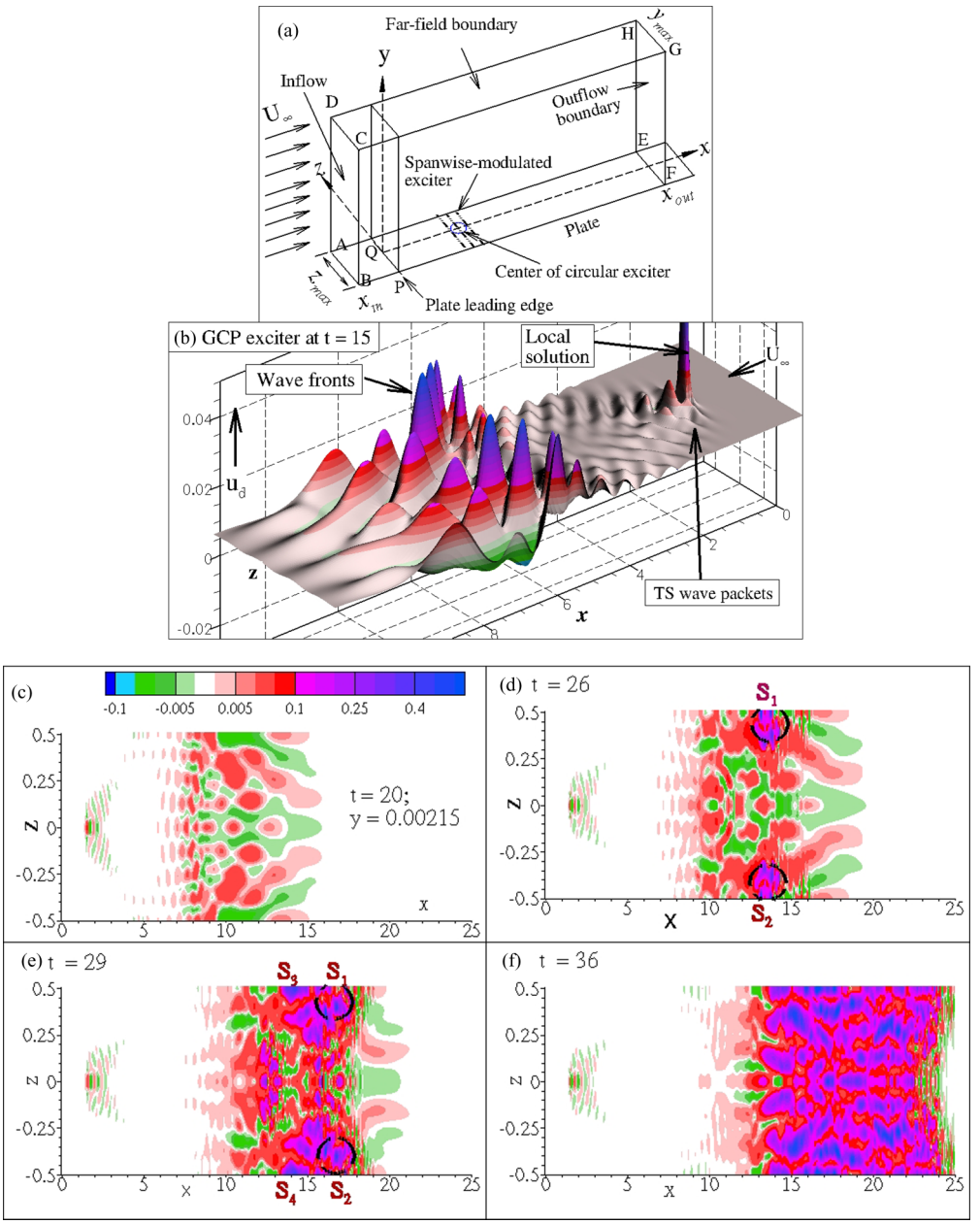

FIG. 2. (Color online) (a) Schematic diagram of a computational domain shown for Gaussian circular patch (GCP) exciter with center located at x_{ex}. (b) Perspective plot of u_d for a height $y = 0.00215$ at $t = 15$ after the onset of excitation for GCP exciter. For this case, $x_{ex} = 1.5$ and amplitude $\alpha_1 = 0.01$ (1% of U_∞). For the GCP exciter, the frequency is $F = 0.5 \times 10^{-4}$. (c)–(f) Plan view of u_d for $y = 0.00215$ and indicated times shown for GCP exciter case described in the legend of Fig. 2(b).

are explained in Ref. [22], as to identify vortical structures in 3D flow-fields. In Fig. 3, trailing part of the STWF is focused to show the later stages of transition and to note the formation of staggered Λ-type vortices. The darker spots on the right side of the frame denote the ringlike elements at the top of the Λ vortices, which have been reported in the literature. This case of computation reported here is due to monochromatic excitation only.

B. Formation of spots during transition

Next, we investigate the formation of turbulent spots and the consequent creation of fully developed turbulent flow, for the case of GCP exciter with $F = 0.5 \times 10^{-4}$. In Fig. 4, we show the contours of ω_z (spanwise component of vorticity) at the indicated time instants, along the midspan location, $z = 0$. At $t = 30$, an intermittent turbulent zone spans from $x \simeq 13$ to 19. With passage of time, one notes the front of this highly perturbed zone to move in the downstream direction, at a speed which is lower but which is of the order of the free-stream velocity. The trailing edge of the STWF shows very minor movement in the downstream direction up to $t = 35$. Beyond that time, this location of the trailing edge of the STWF remains almost frozen at $x \simeq 13$. The transitional flow, which spans from $x \simeq 12$ to 15 in Fig. 4(b), keeps elongating, while causing vortical eruptions from the wall. This transitional flow region

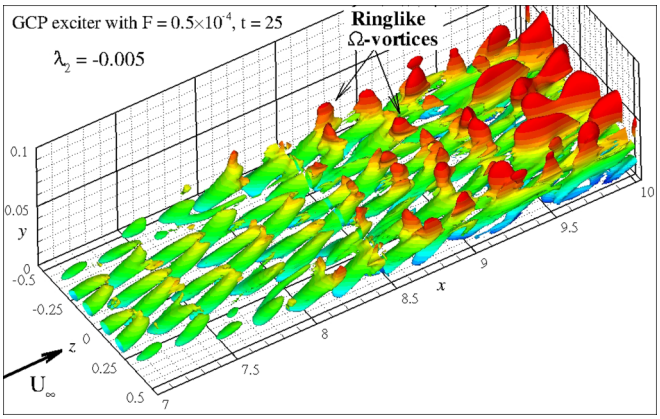

FIG. 3. (Color online) Perspective view of vortical structures created by a Gaussian circular patch excitation case with $\lambda_2 = -0.005$ isosurface shown in (x,z) plane corresponding to $F = 0.5 \times 10^{-4}$.

grows and merges with the turbulent part ahead of it. One such set of vortical eruptions is marked as A in Figs. 4(b) and 4(c). One also notes thickening of the boundary layer, gradually from the laminar value at $x = 12$ to 15 (which can be construed as the point of transition) and beyond for later times. The

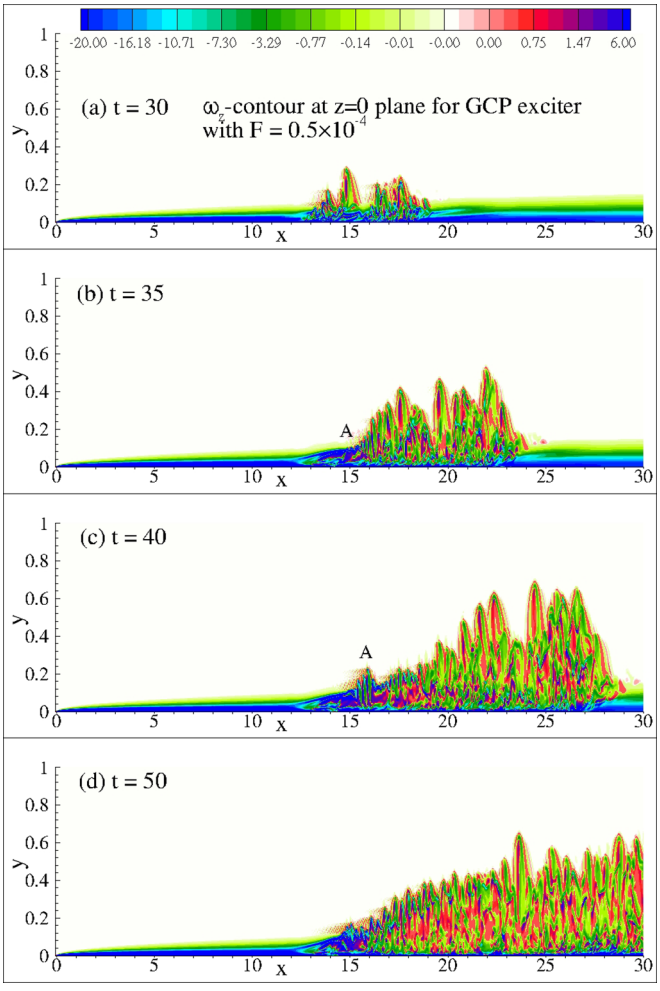

FIG. 4. (Color online) Spanwise vorticity (ω_z) contours shown in midspan location ($z = 0$) in (x,y) plane for the indicated times for the case described in the legend of Fig. 3.

intermittent zone is characterized by highly unsteady vortical eruptions. Presence of unsteady vortical eruptions and constant regeneration mechanism was also noted for deterministically created 2D turbulent flow in Ref. [8]. In Fig. 4(d), the flow is seen to be turbulent beyond $x = 15$; however, the intermittency is lower beyond $x \simeq 25$.

In Figs. 5(a)–5(c), the skin friction coefficient (C_f) variation for the section along $z = 0$ are shown with the streamwise coordinate x, for the indicated times. For zero-pressure-gradient laminar flows, skin friction coefficient varies as $C_f = 0.664 \times \mathrm{Re}_x^{-1/2}$, where Re_x is Reynolds number based on streamwise coordinate x and is shown in the frames as dashed line. For fully developed turbulent boundary layer, time-averaged skin friction coefficient for zero-pressure-gradient flow varies as $\langle C_f \rangle = 0.74 \times \mathrm{Re}_x^{-1/5}$, as given in Refs. [23,24]. This line is shown in all the frames by dash-dotted line. The passage of the STWF is clearly evident in all the frames, indicating highly intermittent flow with the value of C_f fluctuating significantly. When we plot $\langle C_f \rangle$ in Fig. 5(d) (data averaged between $t = 40$ and 50) as a function of x, we note that in the central part of the turbulent spot, the time-averaged C_f displays good match with the turbulent boundary layer value. It is interesting to note that near the location of $x \simeq 14$, $\langle C_f \rangle$ shows a dip and this is due to the onset of unsteady separation associated with transition. This is shown in the stream trace plot shown in Fig. 5(e).

In Fig. 6, corresponding influence on other integrated boundary layer properties are shown in terms of the displacement and momentum thickness (δ^* and θ) at the indicated times, in the left column. In the right column of this figure, the variation of the shape factor ($H = \delta^*/\theta$) as a function of Reynolds number, based on current length is shown. In these frames, the dashed lines indicate the typical values of laminar (top) and turbulent flows (bottom). Once again, one notices an excellent match with the known experimental and theoretical trends for these quantities.

C. Spectrum of inhomogeneous turbulent flow over flat plate

In Fig. 7, compensated energy spectra as defined in Ref. [25] by E_{11}, E_{22}, and E_{33}, are shown along three spanwise locations given by, $z = 0.0$, 0.38, and 0.48, in the different frames. These are obtained by squaring the Fourier-Laplace transform of u_d, v_d, and w_d, respectively. The compensation applied to individual components is due to variation noted for homogeneous turbulence. Thus, the plotted values show deviation from the homogeneous isotropic turbulence value given by the theory due to Kolmogorov [24]. From this figure one notes the existence of an intermediate wavenumber region where spectral densities vary as $k_x^{-5/3}$—a variation in the inertial subrange predicted for 3D isotropic homogeneous turbulence. More importantly, displayed computed spectra show similarity with the experimental data for inhomogeneous flows in Ref. [25]. In this latter reference, local isotropy of the boundary layer about the streamwise wavenumber (k_x) is explored experimentally. Thus, the STWF is noted to take the flow all the way from receptivity stage to fully developed turbulent flow stage, similar to 2D cases reported earlier in Ref. [8]. The fact that the present computations also match the experimental results for inhomogeneous flows [25] establishes

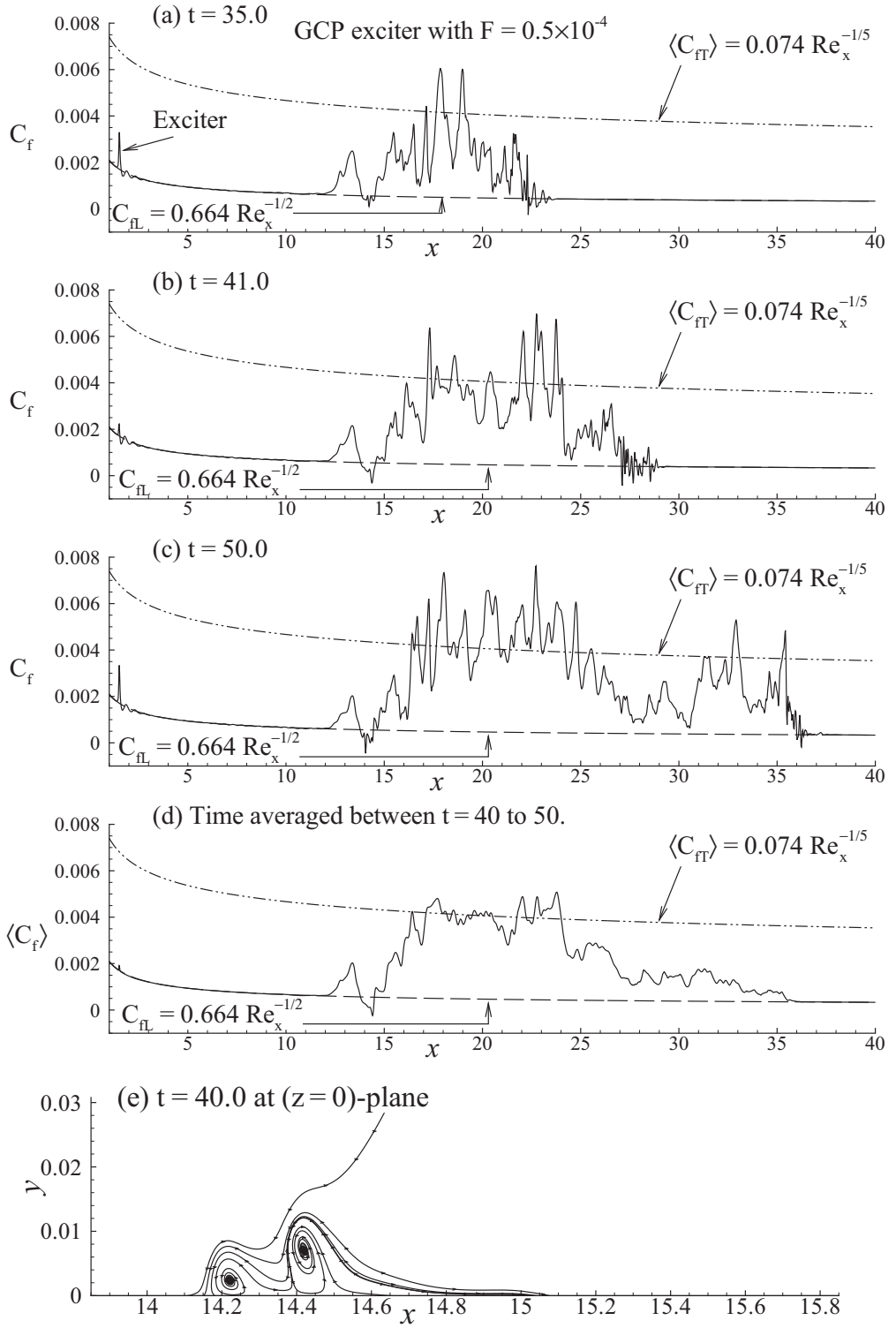

FIG. 5. (a)–(c) Instantaneous and (d) time-averaged skin friction coefficient C_f along midspan, $z = 0$, plotted as function of x. Time averaging of data in (d) is performed during $t = 40$ and 50. Corresponding data for laminar and turbulent flows are indicated by dashed and dash-dotted lines, respectively. In frame (e), stream traces are shown at $t = 40$ to include recirculation region at the onset of transition.

that the STWF is the precursor of turbulence, which takes the 2D equilibrium flow, all the way from the receptivity stage to the final 3D turbulent flow stage. The STWF as an unit process in causing transition from laminar to turbulent flow stage is now fully established for both 2D and 3D turbulence.

V. CONCLUSION

In conclusion, the present study of the process of transition for a zero-pressure-gradient boundary layer by deterministic wall excitation helps us understand the cause by which turbulence in wall-bounded flows is created. Presented results

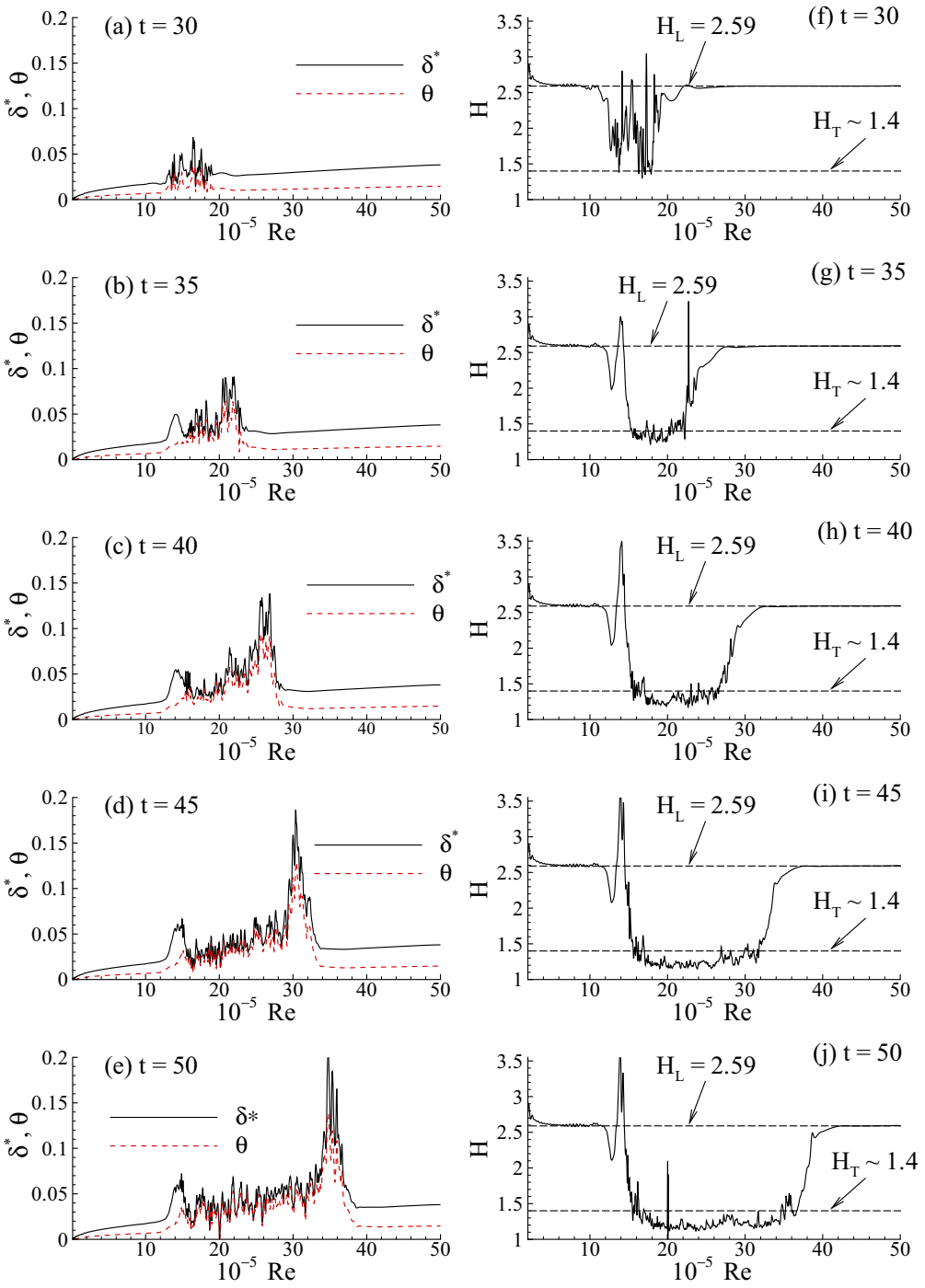

FIG. 6. (Color online) (a)–(e) Displacement thickness (δ^*) and momentum thickness (θ) plotted along midspan ($z = 0$) for the indicated time instants. In frames (f)–(j), the shape factor (H) is plotted along midspan for the corresponding time instants. Here, $H_L = 2.59$ and $H_T \approx 1.4$ are the values of shape factor H for laminar and turbulent zero pressure gradient flows over a flat surface, respectively [23].

here and in Refs. [8,11] identify the unit process of transition to turbulence to be the spatiotemporal wavefront (STWF) for both 2D and 3D routes of transition [26], for small excitation levels. The STWF follows from a complete spatiotemporal description of the perturbation field and is therefore more generic than the conventional spatial or temporal description of the problem. Once a STWF is created by linear mechanism, subsequent linear growth is followed by nonlinear effects, which cause the STWF to display regeneration mechanism. Following nonlinear actions lead to turbulent spots, which merge together to develop into fully developed turbulent flow. Thus, the STWF needs to be created only once and this will create other STWFs via the nonlinear process as the regeneration mechanism. In the presented study here, this was created by the finite start-up of the time-harmonic wall excitation. This can also be augmented by any other discontinuous changes in the excitation pattern.

In terms of specific routes, both K- and H-type transitions in 3D field are triggered by monochromatic excitation via the growth of STWF, with the latter occurring for lower frequency

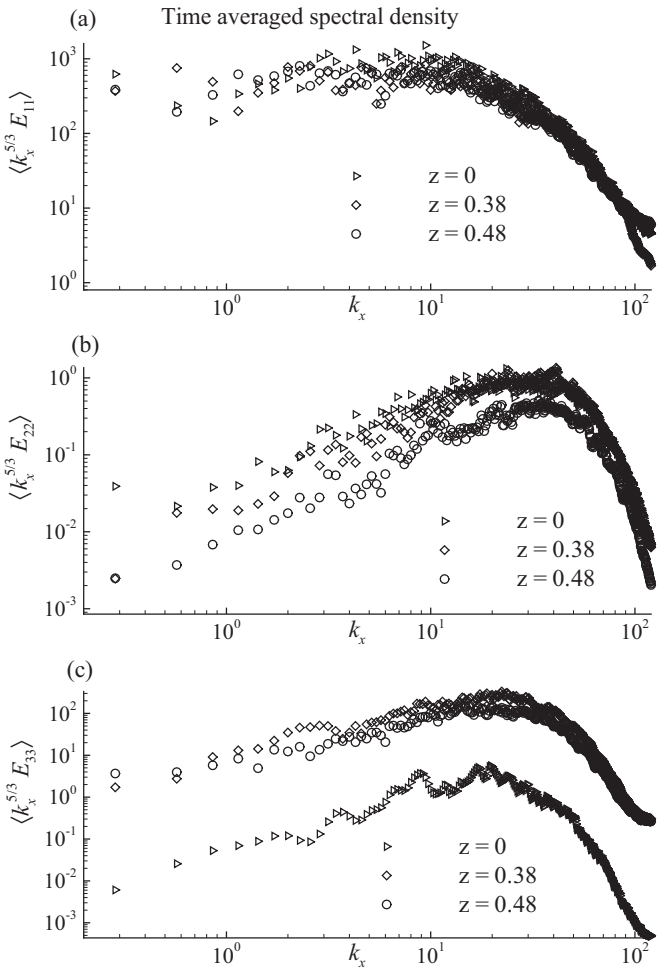

FIG. 7. Time-averaged compensated streamwise spectral density for (a) streamwise, (b) wall-normal, and (c) spanwise velocity components plotted as a function of streamwise wavenumber, k_x, for the indicated spanwise stations, $z = 0$, 0.38, and 0.48 for the GCP excitation cases.

of excitation. These results would be presented elsewhere. This is in contrast to the viewpoint for H-type transition to occur via triad resonant interaction of TS waves. Present work unambiguously establishes that the STWF is the unit process of transition for both 2D and 3D transition created by small excitation associated with moderate to high frequency of excitation, and not by the growth of TS wavepackets. Present results, along with that in Ref. [8], obtained by solving Navier-Stokes equation without any modifications to the governing equation, or using any models, explain how turbulence is created in fluid flows via the growth of the STWF, for both 2D and 3D routes of transition to turbulence.

ACKNOWLEDGMENTS

We are highly indebted to Dr. Mudkavi for various discussions and providing computational resources at 300 Tera-Flop machine at CSIR-NAL, Bangalore. We also acknowledge the computational support provided by the HPC facility at IIT Kanpur and National Supercomputing Facility at CDAC, Pune to carry out the 3D simulations.

APPENDIX A: DIFFERENT FORMULATIONS USED FOR DIRECT NUMERICAL SIMULATION (DNS)

With the advent of computing power, various DNS reported in the literature have used different formulations. DNS of flows reported in the literature [27,28] have earlier used modifications of the governing NSE, some of which are described here. There are various numerical techniques like introducing hyper- and hypoviscosity terms; using distributed deterministic and random body forces are some of the means employed to solve NSE via DNS. While there are also other references [10,15,16], including the present effort, which have reported using unaltered NSE to simulate the classical transition experiment of Ref. [2].

In one of the derived variable formulations given in Ref. [27], the following equation is solved

$$\frac{\partial \omega}{\partial t} - J[\psi,\omega] = \nabla \times \vec{f} + \nu(-1)^{p+1}(\nabla^2)^p \omega - \alpha\omega. \quad \text{(A1)}$$

Here, ψ is the stream function and ω is the vorticity as the dependent variable. In Eq. (A1), J is the Arakawa-Jacobian operator given by $J = (\partial\psi/\partial x)(\partial\omega/\partial y) - (\partial\psi/\partial y)(\partial\omega/\partial x)$. For NSE, the right-hand side of the above equation should only have the second term with $p = 1$. Instead, the right-hand side has the applied Gaussian and white-noise-distributed force given by $\vec{f}$, and the last term is an added damping term with α as the damping frequency. In this reference, $p = 8$ is taken, which implies that the viscous diffusion is overemphasized at higher wavenumbers and is hence known as the hyperviscosity term.

Similarly in Ref. [28] in reporting results for homogeneous, stationary 2D turbulence, the following equation has been solved:

$$\frac{D\omega}{Dt} = \frac{\partial \omega}{\partial t} + J[\psi,\omega] = D + F, \quad \text{(A2)}$$

where F is the forcing term acting at large scale. The term D represents generalized damping term given by

$$D = \mu\nabla^{-2}\omega + \nu\nabla^2\omega.$$

While the second term on the right-hand side is due to viscous diffusion, the first term has been termed by the authors as "physically artificial hypoviscosity."

In solving inhomogeneous problems, some researchers have used the spectral formulation, which requires periodicity in the streamwise direction. For example, in Ref. [29] the following primitive variable formulation is used:

$$\frac{\partial u_i}{\partial t} + u_j\frac{\partial u_i}{\partial x_j} = -\frac{1}{\rho}\frac{\partial p}{\partial x_i} + \nu\frac{\partial^2 u_i}{\partial x_j^2} + F_i. \quad \text{(A3)}$$

To circumvent the nonphysical requirement of periodicity in the streamwise direction, a fringe zone is added—as shown in Fig. 8–where the term F_i is needed inside the fringe zone to enforce periodicity. Thus, in Eqs. (A1) and (A3), one notes the formulations for NSE as used for different numerical approaches.

In Refs. [8,11], NSE is solved also in (ψ,ω) formulation in transformed (ξ,η) plane given by

$$h_1h_2\frac{\partial \omega}{\partial t} + h_2u\frac{\partial \omega}{\partial \xi} + h_1v\frac{\partial \omega}{\partial \eta} = \frac{1}{\mathrm{Re}_L}\nabla^2\omega, \quad \text{(A4)}$$

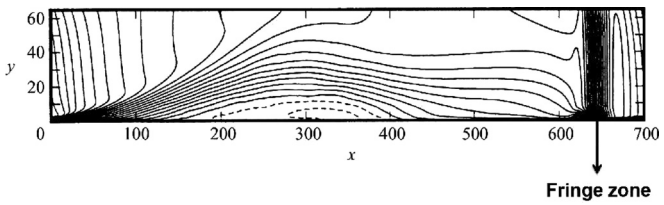

FIG. 8. The domain and fringe zone used in Ref. [29]. The figure is taken from Ref. [29].

where h_1 and h_2 are the scale factors of transformation, and all details are given in Ref. [11] regarding notations. In this formulation, governing equations are solved without any modifications. The disadvantage with this formulation is that this is restricted to 2D flows.

For 3D flows, one can instead solve NSE in $(\vec{V},\vec{\Omega})$, velocity-vorticity formulation, as reported in Refs. [15,16,30]. The same formulation is used here to study 3D transition routes. All computations reported here are performed using velocity-vorticity formulation due to its properties explained in Refs. [31–33]. Governing equations are nondimensionalized using U_∞, L, and L/U_∞ as the velocity, length, and time scales, respectively. Here, U_∞ is the free stream speed, so that the Reynolds number ($\mathrm{Re}_L = U_\infty L/\nu$) based on these scales is chosen as 10^5 for the reported calculations.

Note that in Refs. [10,15,16] a computational domain is used which did not include the leading edge. The computational domain is given as $x_{\text{in}} \leqslant x \leqslant x_{\text{out}}$ along the streamwise direction with $x = 0$ denoting the leading edge; $0 \leqslant y \leqslant y_{\max}$ along the wall-normal direction and $-z_{\max}/2 \leqslant z \leqslant z_{\max}/2$ along the spanwise direction. The origin of the coordinate system is placed at the center of the leading edge of the plate. In Refs. [8,11], the length of computational domain is given by $x_{\text{out}} = 120$ for the 2D problem. In the present computations, this is taken as $x_{\text{out}} = 50$, as compared to the domain length taken in Ref. [10] as 10, which is inadequate to capture the nonlinear evolution of the STWF.

Here, the vorticity transport equation is obtained from incompressible NSE given as

$$\frac{\partial\vec{\Omega}}{\partial t} + \nabla\times(\vec{\Omega}\times\vec{V}) = \frac{1}{\mathrm{Re}_L}\nabla^2\Omega, \tag{A5}$$

where $\vec{\Omega} = (\omega_x,\omega_y,\omega_z)$ is the vorticity vector and $\vec{V} = (u,v,w)$ is the velocity vector. As by definition $\Omega = \nabla\times\vec{V}$, the vorticity vector is solenoidal, i.e., $\nabla\cdot\Omega = 0$. To preserve the solenoidality of the computed vorticity field, in the reported simulations we use the rotational variant of the $(\vec{V},\vec{\Omega})$ formulation of NSE as described in Refs. [30,34]. Following the vector notation, the vorticity transport equation in this formulation is given as

$$\frac{\partial\vec{\Omega}}{\partial t} + \nabla\times\vec{H} = 0, \tag{A6}$$

where $\vec{H} = (\vec{\Omega}\times\vec{V} + \frac{1}{\mathrm{Re}_L}\nabla\times\vec{\Omega})$. The simulations are performed in the transformed (ξ,η,ζ) plane, where $x = x(\xi)$, $y = y(\eta)$, and $z = z(\zeta)$ to have finer resolution near the wall and the leading edge of the plate. In the transformed plane, the individual equations for the vorticity components from Eq. (A6) are

$$\frac{\partial\omega_x}{\partial t} + \left(\frac{1}{h_2}\frac{\partial f_\zeta}{\partial\eta} - \frac{1}{h_3}\frac{\partial f_\eta}{\partial\zeta}\right) = 0, \tag{A7}$$

$$\frac{\partial\omega_y}{\partial t} + \left(\frac{1}{h_3}\frac{\partial f_\xi}{\partial\zeta} - \frac{1}{h_1}\frac{\partial f_\zeta}{\partial\xi}\right) = 0, \tag{A8}$$

$$\frac{\partial\omega_z}{\partial t} + \left(\frac{1}{h_1}\frac{\partial f_\eta}{\partial\xi} - \frac{1}{h_2}\frac{\partial f_\xi}{\partial\eta}\right) = 0, \tag{A9}$$

where h_1, h_2, and h_3 are the scale factors of the transformation given by $h_1 = \partial x/\partial\xi$, $h_2 = \partial y/\partial\eta$, and $h_3 = \partial z/\partial\zeta$. In Eqs. (A7) to (A9), the terms f_ξ, f_η, and f_ζ are given by

$$f_\xi = (w\omega_y - v\omega_z) + \frac{1}{\mathrm{Re}_L}\left(\frac{1}{h_2}\frac{\partial\omega_z}{\partial\eta} - \frac{1}{h_3}\frac{\partial\omega_y}{\partial\zeta}\right), \tag{A10}$$

$$f_\eta = (u\omega_z - w\omega_x) + \frac{1}{\mathrm{Re}_L}\left(\frac{1}{h_3}\frac{\partial\omega_x}{\partial\zeta} - \frac{1}{h_1}\frac{\partial\omega_z}{\partial\xi}\right), \tag{A11}$$

$$f_\zeta = (v\omega_x - u\omega_y) + \frac{1}{\mathrm{Re}_L}\left(\frac{1}{h_1}\frac{\partial\omega_y}{\partial\xi} - \frac{1}{h_2}\frac{\partial\omega_x}{\partial\eta}\right). \tag{A12}$$

In this formulation, the corresponding velocity field is obtained by solving the velocity Poisson equations $\nabla^2\vec{V} = -\nabla\times\vec{\Omega}$, which are given in transformed plane as

$$\nabla^2_{\xi\eta\zeta}u = \left(h_1h_2\frac{\partial\omega_y}{\partial\zeta} - h_3h_1\frac{\partial\omega_z}{\partial\eta}\right), \tag{A13}$$

$$\nabla^2_{\xi\eta\zeta}v = \left(h_2h_3\frac{\partial\omega_z}{\partial\xi} - h_1h_2\frac{\partial\omega_x}{\partial\zeta}\right), \tag{A14}$$

$$\nabla^2_{\xi\eta\zeta}w = \left(h_3h_1\frac{\partial\omega_x}{\partial\eta} - h_2h_3\frac{\partial\omega_y}{\partial\xi}\right), \tag{A15}$$

with the diffusion operator $\nabla^2_{\xi\eta\zeta}$ given as

$$\nabla^2_{\xi\eta\zeta} = \frac{\partial}{\partial\xi}\left(\frac{h_2h_3}{h_1}\frac{\partial}{\partial\xi}\right) + \frac{\partial}{\partial\eta}\left(\frac{h_3h_1}{h_2}\frac{\partial}{\partial\eta}\right) + \frac{\partial}{\partial\zeta}\left(\frac{h_1h_2}{h_3}\frac{\partial}{\partial\zeta}\right).$$

The receptivity problem is studied by solving the Poisson equations for u and w components of velocity given by Eqs. (A13) and (A15). The v component (wall-normal component) of the velocity is calculated by integrating the continuity equation from the wall as

$$v(\xi,\eta,\zeta) = v(\xi,0,\zeta) - \int_0^\eta\left[\frac{h_2}{h_1}\frac{\partial u}{\partial\xi} + \frac{h_2}{h_3}\frac{\partial w}{\partial\zeta}\right]d\eta. \tag{A16}$$

Application of this methodology numerically satisfies the velocity solenoidality condition at the discrete nodes of the domain. Additionally, it also imposes the boundary condition on v component of the velocity at the far-field boundary in Fig. 2(a). This procedure saves time for solving the Poisson equation for the v component.

APPENDIX B: NUMERICAL METHODS

In Appendix A, we noted that there are efforts [10,15,16] including the present one, where unaltered NSE has been used to simulate the classical transition experiment of Ref. [2]. In Refs. [8,11], the same approach of using NSE without any

modifications is adopted for simulating 2D turbulence from the first principle. The only difference between Refs. [10,15,16] and Refs. [8,11] to simulate transition experiments [3–5], is the use of a very small domain in the former and the use of high-accuracy dispersion relation preserving (DRP) scheme in the latter, along with usage of multidimensional filter. Two-dimensional flow can be extremely well resolved using high-accuracy computing methods. In a recent 3D flow transition simulation, the authors in Ref. [10] have used implicit and explicit time integration methods with an overlap region in the wall-normal direction, while a small domain is used in the streamwise direction. In the high-performance computing framework used here, overlap region is also needed for the implicit spatial discretization used. While in Ref. [10] explicit spatial discretization has been used, using different time integration schemes very close to the wall also brings in the issue of internal reflection of signals while passing through the overlap region. These numerical issues are discussed briefly here.

The numerical methods employed to solve the 3D receptivity problem require the use of staggered arrangement of variables for higher accuracy [35]. In the staggered arrangement, velocity components (u, v, w) are defined at the center of the elementary cell-surface perpendicular to it, while the vorticity components $(\omega_x, \omega_y, \omega_z)$ are defined at the center of the sides of the elementary cell, which are parallel to it. In this arrangement, optimized version of staggered compact schemes from Ref. [34] are used for midpoint interpolation and evaluation of first derivatives at midpoint locations. These are variants of the original sixth order schemes given in Ref. [36]. The general stencil of the staggered midpoint interpolation scheme is given as

$$\alpha_{\mathrm{I}}\hat{f}_{j-1} + \hat{f}_j + \alpha_{\mathrm{I}}\hat{f}_{j+1} = \frac{a_1}{2}\left(f_{j-\frac{1}{2}} + f_{j+\frac{1}{2}}\right) + \frac{b_1}{2}\left(f_{j-\frac{3}{2}} + f_{j+\frac{3}{2}}\right). \quad \text{(B1)}$$

Similarly, the general stencil of the staggered compact scheme for the evaluation of the first derivative at the midpoint is given as

$$\alpha_{\mathrm{II}} f'_{j-1} + f'_j + \alpha_{\mathrm{II}} f'_{j+1} = \frac{a_2}{h}\left(f_{j+\frac{1}{2}} - f_{j-\frac{1}{2}}\right) + \frac{b_2}{3h}\left(f_{j+\frac{3}{2}} - f_{j-\frac{3}{2}}\right). \quad \text{(B2)}$$

Here, $\hat{f}_j$'s and f'_j's are the values of the midpoint interpolated function and its first derivative at the jth location, respectively, which are calculated from the known $f_{j\pm n/2}$'s at the $(j \pm n/2)$th-locations. In Eq. (B2), h is the uniform grid spacing. To achieve fourth-order accuracy, the interpolation scheme is given by Eq. (B1), with $a_1 = \frac{1}{8}(9 + 10\alpha_{\mathrm{I}})$ and $b_1 = \frac{1}{8}(6\alpha_{\mathrm{I}} - 1)$ obtained in terms of the parameter α_{I}. For the sixth-order accurate scheme, the additional equation fixes $\alpha_{\mathrm{I}} = \frac{3}{10}$.

Similarly, fourth-order accurate scheme for first derivatives is given in Eq. (B2), with $a_2 = (9 - 6\,\alpha_{\mathrm{II}})/8$ and $b_2 = (22\,\alpha_{\mathrm{II}} - 1)/8$ in terms of α_{II}. Using the next-order condition of Taylor series expansion, one obtains the sixth-order scheme by $\alpha_{\mathrm{II}} = 9/62$.

In the present computations, we use optimized version of the fourth-order scheme determined by investigating in the spectral plane for better dispersion relation preservation (DRP) properties. Such optimization yields $\alpha_{\mathrm{I}} = 0.41$ and $\alpha_{\mathrm{II}} = 0.216$ for Eqs. (B1) and (B2), respectively [30,34]. This is here called the OSCS scheme. The resultant scheme, despite being fourth-order accurate, exhibits superior spectral resolution and DRP properties, as shown in Ref. [30]. Second and mixed derivatives appearing in Eqs. (A7) to (A9) are evaluated using repeated applications of Eq. (B2). Second-order central difference is used to discretize the velocity Poisson Eqs. (A13) and (A15), while midpoint method is used to numerically integrate Eq. (A16) in calculating v-component of velocity. The time integration of vorticity transport equations are performed by optimized Runge-Kutta scheme, ORK_3, developed in Ref. [37]. Grid clustering near the leading edge in streamwise direction and near the wall, in the wall-normal direction, are achieved by tangent hyperbolic functions [38]. It has been shown in Ref. [21] that such transformation causes least aliasing error. Uniform grid is chosen along spanwise direction for easy implementation of the periodic boundary conditions.

One notes that sixth-order compact spatial discretization schemes have been used for receptivity problems in Refs. [15,33]. These authors used RK_4 scheme for time integration.

In Ref. [10], the authors have used fourth-order explicit (CD_4) scheme for spatial discretization, as given by Eqs. (2.13) and (2.14) in Sayadi [39], along with the three-stage Runge-Kutta (RK_3) scheme.

In the present work, an explicit four-stage optimized Runge-Kutta method developed with better DRP properties has been used, which also has third-order accuracy, termed as the ORK_3 scheme. The combined space-time discretization method used here is referred to as OSCS-ORK_3 scheme.

In Fig. 9, the numerical properties of the present OSCS-ORK_3 and CD_4-RK_3 schemes are presented, using the model convection equation

$$\frac{\partial u}{\partial t} + c\frac{\partial u}{\partial x} = 0.$$

The utility of this model equation has been exploited not only for pedagogic reason, but also for the realistic reason of developing methods for convection-dominated flow problems in Refs. [21,40] in parallel computation framework. For this nondissipative, nondispersive model equation, the performance parameters are the numerical amplification rate (G), normalized numerical phase speed (c_N/c), and normalized group velocity (V_{gN}/c), as shown in Fig. 9. The convection equation is neutrally stable, hence any numerical method solving it must also be the same. The spatial resolution is measured in terms of nondimensional wavenumber (kh), where h is the uniform spacing and time resolution is measured by the CFL number given by $N_c = c\Delta t/h$. For the nondispersive dynamics of the model equation, one expects that the normalized phase speed and group velocity must take unit value for minimizing dispersion error. When one looks at extreme dispersion error given by the q waves for which $V_{gN}/c < 0$ [21,41], one notices a significantly better state of affairs for OSCS-ORK_3 scheme.

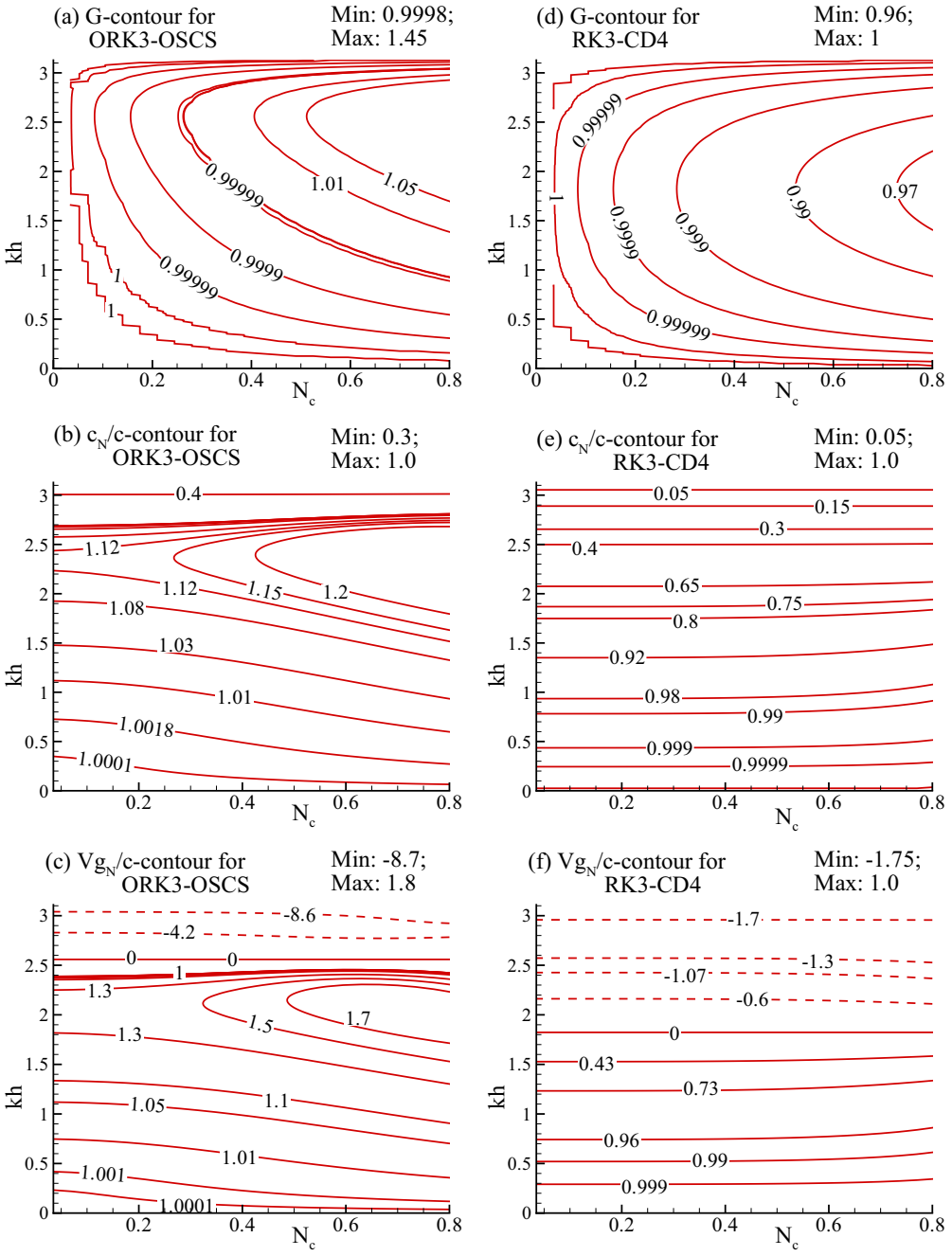

FIG. 9. (Color online) Numerical properties of CD_4-RK_4 method are compared with the present OSCS-ORK_3 method. These are shown for (a, d) numerical amplification factor (G); (b, e) normalized phase speed (c_N/c), and (c, f) normalized group velocity (V_{gN}/c) in (N_c,kh) plane.

Another interesting development is the methods used in Ref. [10], which relates to using explicit and implicit time integration methods together. In this work, a very thin layer close to the wall is considered where second-order accurate implicit Crank-Nicolson scheme is applied to overcome the restriction on numerical time-step posed by the fine wall-normal resolution at the wall for explicit methods. Above this layer, the time integration is switched to classical RK_3 method. It is well known that explicit methods commit less error as compared to implicit methods and this is the motivation for the switch over from one to the other. An overlapping region of six points have been taken in Ref. [10] for the switch over from implicit to explicit method of time integration. In actual practice, one only requires two points overlap between the two zones for explicit schemes for spatial discretization.

In parallel computing, one is also forced to use overlap region for compact schemes as employed here. The reason and deciding upon number of overlap points for the developed parallel compact scheme using Schwartz domain decomposition is discussed in detail in Ref. [42] and is not reported here. It was noted that for the passage of wave-packets, at least six overlap points are needed for the model 1D convection equation. Usage

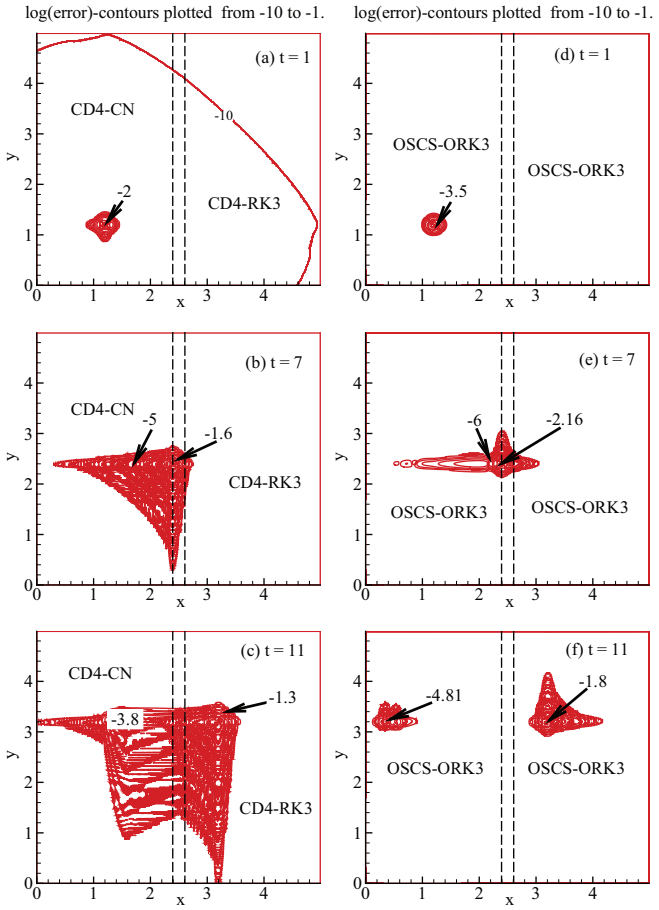

FIG. 10. (Color online) Numerical solution of 1D convection equation by (a)–(c) combination of Crank-Nicolson and CD_4 schemes used on the left of the overlap region and CD_4-RK_3 method on the right [10] is compared with the results of present OSCS-ORK_3 method shown in frames (d)–(f). In Ref. [10], six-point overlap is used, while ten-point overlap is used for the compact scheme.

of compact scheme for spatial discretization of NSE requires larger overlap region and in the present exercise, ten points overlap is used. Thus, the need to use overlap region for parallel compact scheme and for IMEX methods are different. Yet, it is important to investigate resultant effects, as shown in Fig. 10.

To understand effects of the overlap regions employed due to spatial discretization by parallel compact scheme [42] here and for the IMEX time integration method used in Ref. [10], we have computed the 2D convection equation with a wavepacket as the initial condition moving at an angle of 45° to the x axis. The initial condition is given by

$$u(x,y,t=0) = \exp[-500s]\,\cos s,$$

where $s^2 = (x-x_0)^2 + (y-y_0)^2$, and s is along the oblique direction of signal propagation. In a domain $0 \leqslant x \leqslant 5$, $0 \leqslant y \leqslant 5$, the packet is initially placed at $x_0 = y_0 = 1.6$, with the phase speed components $c_x = 0.2$ and $c_y = 0.2$ in x and y directions, respectively. For the computations, a grid with 500×500 points is used and time step is fixed using the CFL number of 0.1. Thus, one can obtain the error and plot it as a function of time, as shown in Fig. 10 for the indicated methods. In this figure, the magnitude is shown in terms of the exponent of error. It is readily noted that any method displays dispersion, which causes large error in the neighborhood of the wavepacket, which shows the maximum exponent in all the frames that keeps growing with time. However, when the wavepacket goes through the overlap region, it causes another error packet moving upstream due to the switch-over from one subdomain to another. The error committed by the compact scheme is at least one order lower as compared to the IMEX scheme. Moreover, the region over which the error gets smeared behind the advancing wavepacket becomes larger in area and magnitude for the IMEX method.

Hence, if a computation is performed in a small domain, then once the STWF convects out of the computational domain there is no possibility of regeneration of the STWFs, as seen in Refs. [8,11]. This is confirmed by calculations (not reported) that even CD_4-RK_4 method produces the STWF and follows the same train of events reported in Refs. [8,11]. Thus, the transition occurring in zero-pressure-gradient boundary layer by time-harmonic excitation depicted in these references is the unit process for the experiment performed in Ref. [2]. Present computations (for 3D route) and those in Refs. [8,11] showcase this unit process, to provide an understanding of the physical mechanism behind transition.

The authors of Ref. [10] added random excitation along with the time-harmonic wall excitation. Such random excitation created repeated numerical packets that contaminate the flow, preventing the formation of the distinct STWF. Such random excitation from the wall alone is an artifact and one expects such disturbances in an experimental facility due to free-stream turbulence. Such random wall excitations can trigger turbulence in a very small domain and the results may appear similar to the reported *bypass transition* in Ref. [43]. The ensuing events may mimic the bypass transition reported by vortex convecting downstream, similar to the vortex-induced instability described in Refs. [44,45].

[1] R. Feynman, R. B. Leighton, and M. Sands, *The Feynman Lectures on Physics* (Addison-Wesley, Boston, MA, 1964).
[2] G. B. Schubauer and H. K. Skramstad, J. Aero. Sci. **14**, 69 (1947).
[3] P. S. Klebanoff, K. D. Tidstrom, and L. M. Sargent, J. Fluid Mech. **12**, 1 (1962).
[4] Y. S. Kachanov and V. Y. Levchenko, J. Fluid Mech. **138**, 209 (1984).
[5] Y. S. Kachanov, Ann. Rev. Fluid Mech. **26**, 411 (1994).
[6] T. K. Sengupta, *Instabilities of Flows and Transition to Turbulence* (CRC Press, Taylor & Francis Group, Florida, USA, 2012).
[7] T. K. Sengupta, M. Ballav, and S. Nijhawan, Phys. Fluids **6**, 1213 (1994).
[8] T. K. Sengupta and S. Bhaumik, Phys. Rev. Lett. **107**, 154501 (2011).

[9] T. K. Sengupta, A. K. Rao, and K. Venkatasubbaiah, Phys. Rev. Lett. **96**, 224504 (2006).
[10] T. Sayadi, C. W. Hamman, and P. Moin, J. Fluid Mech. **724**, 480 (2013).
[11] T. K. Sengupta, S. Bhaumik, and Y. G. Bhumkar, Phys. Rev. E **85**, 026308 (2012).
[12] G. I. Taylor, in *Proceedings of the Fifth International Congress on Applied Mechanics*, edited by J. P. Den Hartog and H. Peters (Wiley, New York, 1939).
[13] W. S. Saric, Phys. Fluids: Gallery Fluid Motions **29**, 2770 (1986).
[14] A. D. D. Craik, J. Fluid Mech. **50**, 393 (1971).
[15] W. Würz, D. Sartorius, M. Kloker, V. I. Borodulin, and Y. S. Kachanov, Phys. Fluids **24**, 094103 (2012).
[16] H. F. Fasel, U. Rist, and U. Konzelmann, AIAA J. **28**, 29 (1990).
[17] U. Rist and H. F. Fasel, J. Fluid Mech. **298**, 211 (1995).
[18] L. N. Trefethen, A. E. Trefethen, S. C. Reddy, and T. A. Driscoll, Science **261**, 578 (1993).
[19] F. Alizard and J. Robinet, Phys. Fluids **19**, 114105 (2007).
[20] A. Monokrousos, E. Åkervik, L. Brandt, and D. S. Henningson, J. Fluid Mech. **650**, 181 (2010).
[21] T. K. Sengupta, *High Accuracy Computing Methods: Fluid Flows and Wave Phenomena* (Cambridge University Press, Cambridge, New York, 2013).
[22] J. Jeong and F. Hussain, J. Fluid Mech. **285**, 69 (1995).
[23] H. Tennekes and J. L. Lumley, *A First Course in Turbulence* (MIT Press, Cambridge, MA, 1972).
[24] S. B. Pope, *Turbulent Flows* (Cambridge University Press, Cambridge, UK, 2000).
[25] S. G. Saddoughi and S. V. Veeravalli, J. Fluid Mech. **268**, 333 (1994).
[26] See Supplemental Material at http://link.aps.org/supplemental/10.1103/PhysRevE.89.043018 for perspective and plan views of the evolution of the disturbance streamwise velocity in (x, z) plane for the GCP excitation case reported here.
[27] L. M. Smith and V. Yakhot, J. Fluid Mech. **274**, 115 (1994).
[28] A. Bracco and J. C. McWilliams, J. Fluid Mech. **646**, 517 (2010).
[29] M. Skote and D. S. Henningson, J. Fluid Mech. **471**, 107 (2002).
[30] S. Bhaumik, Ph.D. Thesis, I.I.T. Kanpur, 2013.
[31] N. Takemitsu, J. Comput. Phys. **61**, 499 (1985).
[32] T. B. Gatski, Applied Numer. Math. **7**, 227 (1991).
[33] H. L. Meitz and H. F. Fasel, J. Comput. Phys. **157**, 371 (2000).
[34] S. Bhaumik and T. K. Sengupta, AIAA-2011-3238, Paper presented at the 20th AIAA CFD conference, Hawaii, USA (2011).
[35] H. Huang and M. Li, Comput. Fluids **26**, 59 (1997).
[36] S. Nagarajan, S. K. Lele, and J. H. Ferziger, J. Comput. Phys. **191**, 392 (2003).
[37] T. K. Sengupta, M. K. Rajpoot, and Y. G. Bhumkar, Comput. Fluids. **47**, 144 (2011).
[38] P. R. Eiseman, Ann. Rev. Fluid Mech. **17**, 487 (1985).
[39] T. Sayadi, Ph.D. thesis, Stanford University, 2012.
[40] H. Lomax, T. H. Pulliam, and D. W. Zingg, *Fundamentals of CFD* (Springer Verlag, Berlin, Germany, 2002).
[41] T. K. Sengupta, Y. G. Bhumkar, M. K. Rajpoot, V. K. Suman, and S. Saurabh, App. Math. Comp. **218**, 9035 (2012).
[42] T. K. Sengupta, A. Dipankar, and A. K. Rao, J. Comp. Physics **220**, 654 (2007).
[43] X. Wu and P. Moin, J. Fluid Mech. **630**, 5 (2009).
[44] T. K. Sengupta, S. De, and S. Sarkar, J. Fluid Mech. **493**, 277 (2003).
[45] P. A. Durbin and X. Wu, J. Fluid Mech. **39**, 107 (2007).